Deep Learning-based Multi-scale Monitoring of Drought in China with High Spatial Resolution

Yingying Peng[1], Jun Liu [1,*], Zhihui Wang [1], Man Li [1]

[1] School of informatics, Hunan University of Chinese Medicine, Changsha 410208, China;
- yingyingpeng@hnucm.edu.cn, jun.liu@hnucm.edu.cn, onlywangzh@hnucm.edu.cn, mavisleemm@hnucm.edu.cn
*Correspondence: jun.liu@hnucm.edu.cn

Abstract:

Under the background of global warming, the impacts of extreme climate events are becoming increasingly severe, with drought posing particularly significant threats to both human society and the natural environment. Drought is recognized as the second most devastating natural disaster globally. Characterized by its complexity and variability, identifying, assessing, and predicting drought features remains challenging. The Standardized Precipitation Evapotranspiration Index (SPEI), known for its multi-temporal scale characteristics, can represent various drought types and better reflect changes in drought dynamics. It has been increasingly applied in climatological and hydrological studies. However, using SPEI data with a 0.5-degree resolution to assess drought conditions in localized regions of China yields relatively low accuracy, hindering precise evaluation and prediction of drought severity and trends. Therefore, enhancing the spatial resolution of SPEI data is critically important. This study proposes the High Spatial-Resolution SPEI Network (HSR-SPEINet), which integrates environmental factors and remote sensing reflectance data to generate a 1 km resolution SPEI dataset. Experimental results demonstrate its strong accuracy.

Keywords: Drought, Deep Learning, SPEI, High Spatial Resolution, HSR-SPEINet.

1. Introduction

Drought is a critical natural disaster facing humanity today. Since the 1970s, drought events have been characterized by prolonged duration, extensive spatial coverage, and increasing frequency [1], with growing regions affected by drought impacts [2], making it a globally significant concern. Against the backdrop of escalating human activities and persistent climate change, issues such as water scarcity and global warming have intensified, further exacerbating drought conditions. Based on their impacts, droughts can be categorized into meteorological, hydrological, and agricultural droughts [3][4]. Regardless of type, droughts often lead to severe economic, agricultural, and environmental challenges in affected areas. For instance, in 2011, agricultural losses in Texas, USA, due to drought reached $7.62 billion. In 2019, extreme heat and prolonged drought in Australia fueled wildfires that lasted for over five months, severely impacting local economic development and social stability. Similar events have occurred in northern China, the western United States, India, southern Europe, and other regions [5][6]. Consequently, drought monitoring remains a vital global task.

In China, the economic losses caused by drought are particularly pronounced, as the country ranks among those most severely affected by drought disasters. Recent studies indicate an overall increasing trend in annual arid days nationwide [7][8]. The IPCC assessment report [9] reveals that the boundary between semi-arid and semi-humid regions in China has progressively shifted southward, accompanied by an expansion trend in drought-prone areas [10]. A distinct aridification trend has emerged across northern China, forming a contiguous drying belt stretching from the northeast to the northwest. As a major agricultural nation, China faces acute challenges from drought impacts on crop production, particularly for rain-fed agriculture, where drought significantly reduces yields [11]. These conditions constrain sustainable agricultural development and further threaten economic stability, political security, and social welfare. Since the early 21st century, drought-induced grain losses in China have reached 37.284 million metric tons—double the losses recorded in the 1980s and equivalent to 7.7% of total grain production during that period. Consequently, enhancing the accuracy of drought trend prediction and monitoring indicators holds critical importance for drought early warning systems, economic resilience, and regional ecological environment protection in China [12][13].

Drought monitoring emerged in the early 20th century, driven by the need for systematic assessment and effective surveillance. During this period, various drought indices were progressively developed to quantify drought characteristics across diverse regions. Among drought types, meteorological drought typically precedes other categories, making meteorological indices a widely adopted tool for monitoring and early warning. Approximately 60 meteorological drought indices have been documented, including the Standardized Precipitation Index (SPI) [14], Standardized Precipitation Evapotranspiration Index (SPEI) [15], and Palmer Drought Severity Index (PDSI) [16]. Each index exhibits unique strengths and limitations. For instance, SPI and SPEI are favored for their computational simplicity and multi-temporal scalability [17], enabling robust drought characterization and global applicability. However, SPI solely incorporates precipitation data, limiting its utility in environmentally and topographically complex regions [18]. In contrast, SPEI integrates precipitation and potential evapotranspiration (PET) through a log-logistic distribution normalization process, providing a more comprehensive drought representation [19]. Nevertheless, SPEI demands high-quality input data and may underperform in detecting extreme drought events compared to more sophisticated indices. Given the inherent complexity of drought mechanisms and nonlinear interactions among driving factors [20], traditional meteorological indices remain insufficient for capturing multi-dimensional drought dynamics, necessitating methodological improvements.

The advent of artificial intelligence has facilitated breakthroughs in drought research, particularly in addressing nonlinear relationships among drought drivers. Machine learning (ML) algorithms—such as Support Vector Machines (SVM) [21], Random Forest (RF) [22], Light Gradient Boosting Machine (LightGBM) [23], and Extreme Learning Machines (ELM) [24]—have demonstrated efficacy in drought monitoring. Shen et al. [25] developed an integrated drought monitoring framework using RF, while Achite et al. [26] combined

vegetation, precipitation, and topographic factors via classification and regression methods to formulate a Synthetic Drought Index (SDI). Despite these advances, ML-based approaches face challenges, including stringent data quality requirements, dependency on large training datasets, and limited generalizability in data-scarce drought monitoring scenarios. Additionally, ML models struggle to extract high-level features when processing high-dimensional input parameters [27][28].

Deep learning (DL), a neural network-driven subset of machine learning, has surpassed conventional ML methods in numerous applications. Prodhan et al. [28] employed a Deep Feedforward Neural Network (DFNN) with remote sensing data to predict agricultural drought in South Africa, outperforming distributed RF and gradient boosting models. Similarly, Balti et al. [29] demonstrated the superiority of Long Short-Term Memory (LSTM) networks over ARIMA and Prophet models in forecasting SPEI for Jiangsu Province, China. DL addresses key limitations in drought monitoring through techniques such as data augmentation [30][31] and transfer learning [32], which mitigate data scarcity issues. Furthermore, attention mechanisms [33][34] enhance feature extraction capabilities, enabling DL models to capture intricate drought-related patterns from complex datasets. The hierarchical architecture of DL networks also facilitates the modeling of nonlinear interactions among drought drivers.

Given the multi-factor, nonlinear, and data-intensive nature of drought dynamics, traditional meteorological indices and ML methods exhibit inherent constraints in monitoring tasks. This study focuses on investigating the application of deep learning methodologies to advance drought monitoring capabilities, addressing existing gaps through innovative computational frameworks.

2. Related Work

The computational procedure for SPEI is as follows:

Step 1: Calculate potential evapotranspiration (PET). The modified Hargreaves method was employed to compute PET.

$$\mathrm{PET} = 0.0013 \times 0.408 R_a \times (T_{avg} + 17.0) \times (TD - 0.0123P)^{0.76} \quad (1)$$

Step 2: Calculate the monthly difference between precipitation and evapotranspiration. The specific formula is defined as:

$$D_i = P_i - PET_i \quad (2)$$

where D_i represents the difference between precipitation and evapotranspiration, P_i denotes monthly precipitation, and PET_i is monthly evapotranspiration.

Step 3: Fit the water balance time series D using a three-parameter log-logistic probability distribution. The probability density function of the log-logistic distribution is expressed as:

$$F(x) = [1 + (\frac{\alpha}{x-\gamma})^{\beta}]^{-1} \quad (3)$$

α , β , γ represent the scale parameter, shape parameter, and location parameter, respectively. These parameters are estimated using the L-moments method, formulated as:

$$\alpha = \frac{(w_0 - 2w_1)\beta}{\Gamma(1+1/\beta)\Gamma(1-1/\beta)} \quad (4)$$

$$\beta = \frac{2w_1 - w_0}{6w_1 - w_0 - 6w_2} \quad (5)$$

$$Y = w_0 - \alpha\Gamma(1+1/\beta)\Gamma(1-1/\beta) \quad (6)$$

Where Γ represents the gamma function. w_0 , w_1 , w_2 denote the probability-weighted moments of the original data series. The calculation method is defined as follows:

$$w_s = \frac{1}{N}\sum_{i=0}^{N}(1-F_i)^S D_i \quad (7)$$

$$F_i = \frac{i - 0.35}{N} \quad (8)$$

where N denotes the number of months involved in the calculation.

Step 4: Standardize the cumulative probability density:

$$P = 1 - F(x) \quad (9)$$

When the cumulative probability $P \le 0.5$,

$$W = \sqrt{-2\ln p} \quad (10)$$

$$\mathrm{SPEI} = W - \frac{c_0 + c_1 W + c_2 W^2}{1 + d_1 W + d_2 W^2 + d_3 W^3} \quad (11)$$

where c0=2.515517, c1=0.802853, c2=0.010328, d1=1.432788, d2=0.189269, d3=0.001308.

when $P > 0.5$, $P = 1 - P$,

$$\mathrm{SPEI} = -(W - \frac{c_0 + c_1 W + c_2 W^2}{1 + d_1 W + d_2 W^2 + d_3 W^3}) \quad (12)$$

3. Proposed Method

Deep learning achieves the extraction of features from external input data from low-level to high-level by establishing and simulating the hierarchical structure of the human brain, thereby interpreting external data. Compared to traditional learning structures, deep learning emphasizes greater depth in model architecture, typically containing multiple hidden layers. In deep learning, feature learning is crucial, where predictions and recognitions are accomplished through layer-by-layer transformations of features.

Deep learning possesses advantages such as strong learning capability, broad coverage and adaptability, high data-driven potential, excellent portability, direct feature extraction from data, continuous performance improvement with increasing data scale, and applicability to various scenarios. Extensive research has shown that deep learning has achieved outstanding performance in computer vision tasks.

During model training, sample balancing is necessary to improve the model's goodness-of-fit. Since the distribution of SPEI ground-truth values is highly uneven in reality, exhibiting a pattern where intermediate values are more frequent while extreme values are sparse, imbalanced samples can lead to biased learning in algorithms. Therefore, sample balancing before model training is essential. This project adopts a minority oversampling approach: under the condition of uneven SPEI value distribution, underrepresented data samples are repeated, ensuring similar quantities of samples across all severity levels.

This study leverages satellite remote sensing combined with artificial intelligence algorithm libraries to train a high-precision SPEI prediction model using deep learning. Through data gridding and sample balancing, a balanced sample set with 0.5°×0.5° resolution is established. Based on this, regression

relationships between 16 input variables and SPEI values are constructed.

3.1 High Spatial-Resolution SPEI Network (HSR-SPEINet)

The input of the HSR-SPEINet model comprises 16 environmental factors, divided into three components: 8 indices and 7 reflectance values provided as time series inputs $[X_1, X_2, \ldots, X_t]$ and Elevation. The environmental factors X_t consist of vectors [ET, PET, NDVI, EVI, LST, FPAR, LAI, GPP] formed by 8 indices and 7 reflectance values [sur_refl_b01, sur_refl_b02, sur_refl_b03, sur_refl_b04, sur_refl_b05, sur_refl_b06, sur_refl_b07] at time step t, with a monthly time scale, as shown in figure 1. The temporal length is defined based on drought occurrence periods in China from 2004 to 2023, specifically as 1, 3, 6, 9, 12, and 24 months, thereby supplying multi-temporal-scale environmental factor information to the HSR-SPEINet model.

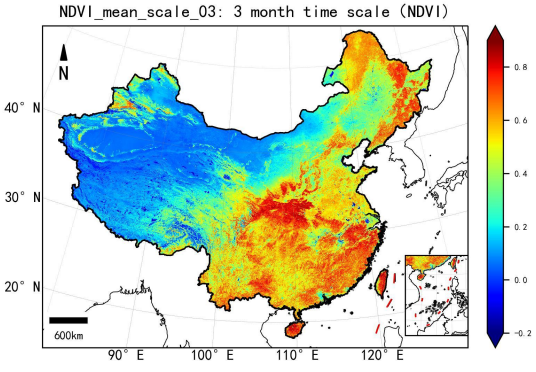

(a)

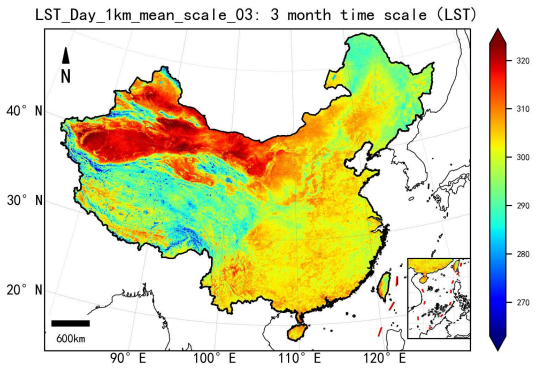

(b)

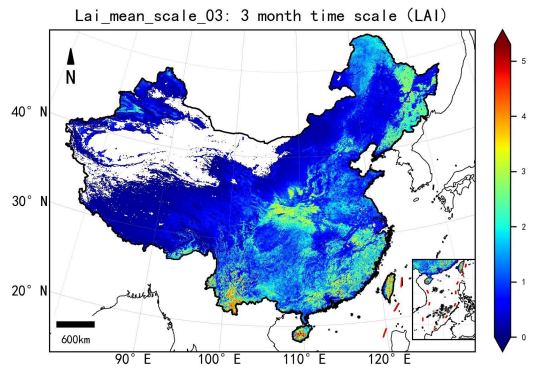

(c)

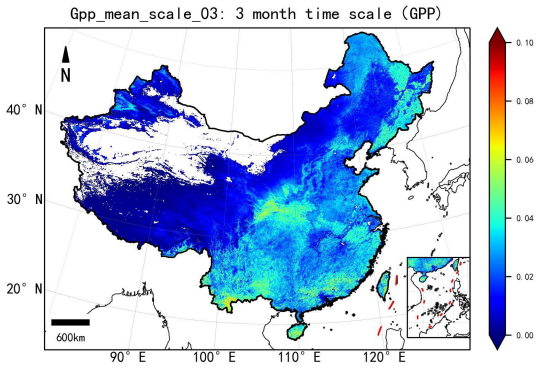

(d)

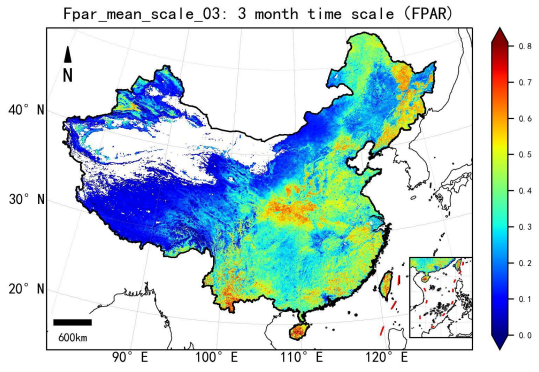

(e)

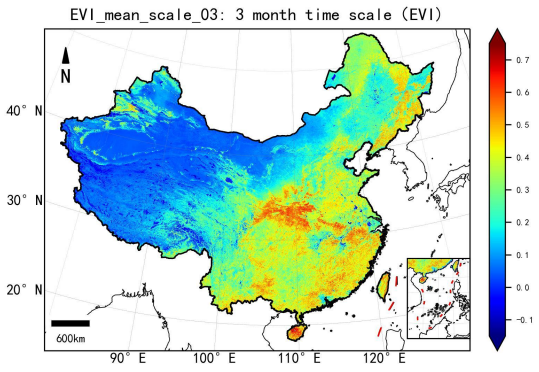

(f)

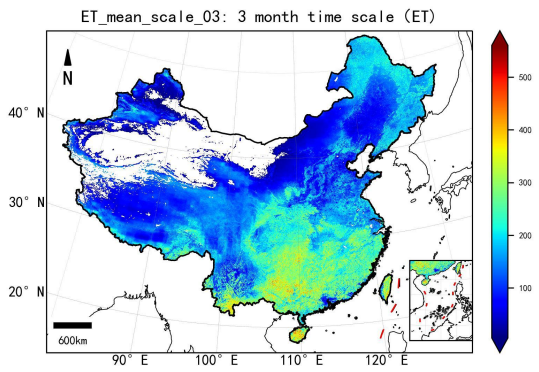

(g)

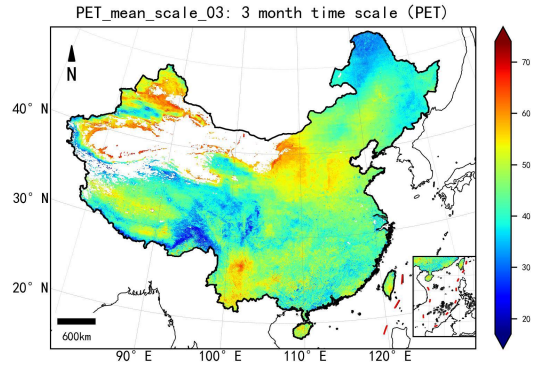
PET_mean_scale_03: 3 month time scale (PET)
N
40° N
30° N
20° N
600km
90° E
100° E
110° E
120° E
70
60
50
40
30
20

(h)

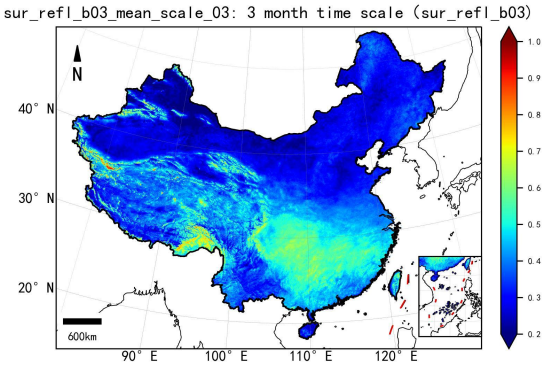
sur_refl_b03_mean_scale_03: 3 month time scale (sur_refl_b03)
N
40° N
30° N
20° N
600km
90° E
100° E
110° E
120° E
1.0
0.9
0.8
0.7
0.6
0.5
0.4
0.3
0.2

(l)

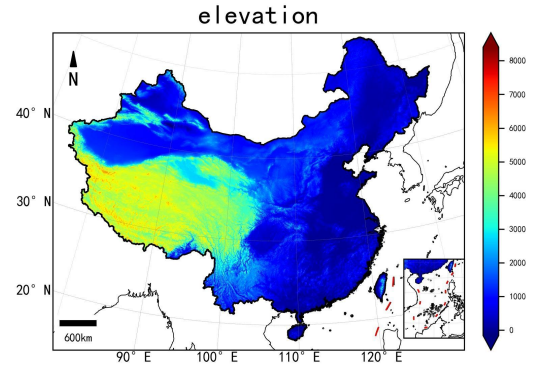
elevation
N
40° N
30° N
20° N
600km
90° E
100° E
110° E
120° E
8000
7000
6000
5000
4000
3000
2000
1000
0

(i)

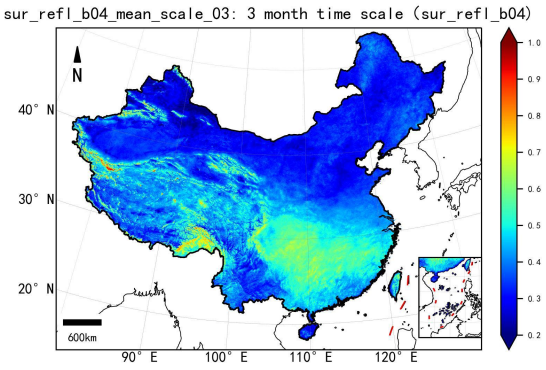
sur_refl_b04_mean_scale_03: 3 month time scale (sur_refl_b04)
N
40° N
30° N
20° N
600km
90° E
100° E
110° E
120° E
1.0
0.9
0.8
0.7
0.6
0.5
0.4
0.3
0.2

(m)

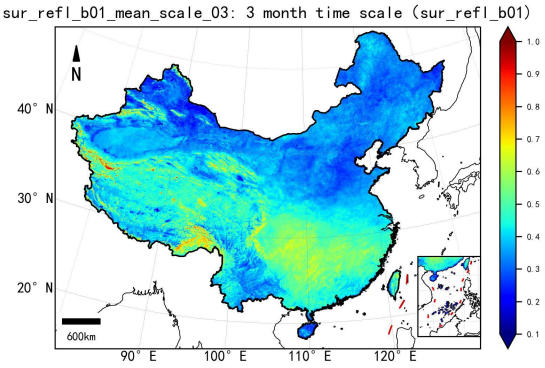
sur_refl_b01_mean_scale_03: 3 month time scale (sur_refl_b01)
N
40° N
30° N
20° N
600km
90° E
100° E
110° E
120° E
1.0
0.9
0.8
0.7
0.6
0.5
0.4
0.3
0.2
0.1

(j)

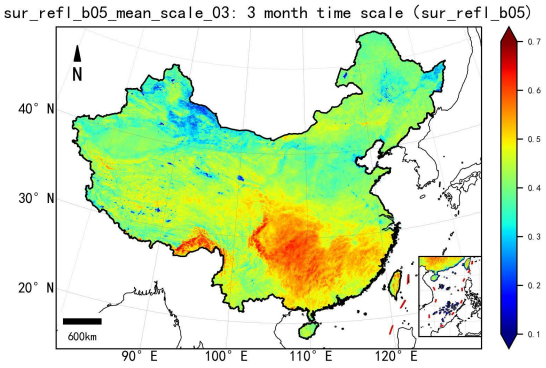
sur_refl_b05_mean_scale_03: 3 month time scale (sur_refl_b05)
N
40° N
30° N
20° N
600km
90° E
100° E
110° E
120° E
0.7
0.6
0.5
0.4
0.3
0.2
0.1

(n)

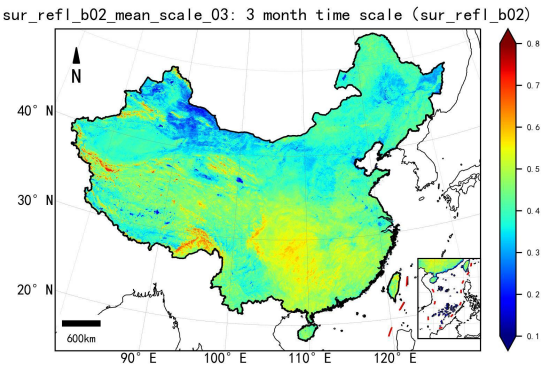
sur_refl_b02_mean_scale_03: 3 month time scale (sur_refl_b02)
N
40° N
30° N
20° N
600km
90° E
100° E
110° E
120° E
0.8
0.7
0.6
0.5
0.4
0.3
0.2
0.1

(k)

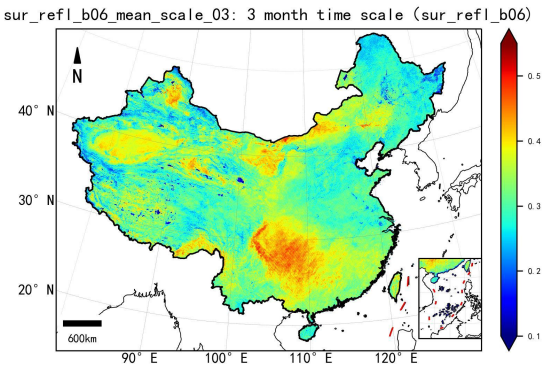
sur_refl_b06_mean_scale_03: 3 month time scale (sur_refl_b06)
N
40° N
30° N
20° N
600km
90° E
100° E
110° E
120° E
0.5
0.4
0.3
0.2
0.1

(o)

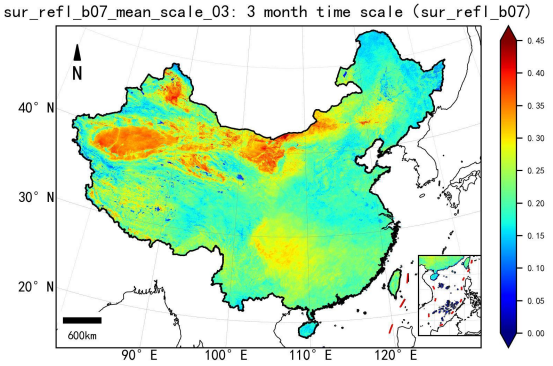

(p)

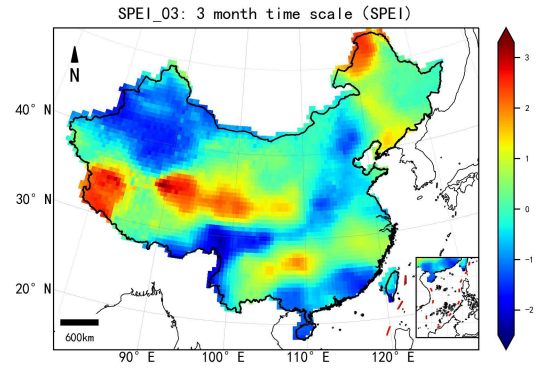

(q)

Fig.1 16 feature data on a one-month time scale in June 2021. (a) NDVI (b) LST (c) LAI (d) GPP (e) FPAR (f) EVI (g) ET (h) PET (i) elevation (j) sur_ref_b01 (k) sur_ref_b02 (l) sur_ref_b03 (m) sur_ref_b04 (n) sur_ref_b05 (o) sur_ref_b06 (p) sur_ref_b07 (q) SPEI.

3.2 Spatiotemporal Feature Extraction Module

Unlike traditional deep learning methods, which typically use a single neural network for feature extraction of all inputs, this study employs different network structures for feature extraction based on the input of "8 indices + 7 reflectance values + elevation." For the time-series input of "8 indices + 7 reflectance values," the HSR-SPEINet model uses ALSTM (Attention-based Long Short-Term Memory) to extract temporal features. For the elevation input, the HSR-SPEINet model applies an Artificial Neural Network (ANN) to extract static spatial features.

The proposed ALSTM comprises 3 LSTM layers and 1 attention layer constructed by a fully connected neural network. The three LSTM layers enable the model to hierarchically extract high-level abstract temporal features from the input time-series data. Due to its unique gating mechanism, LSTM selectively extracts effective information from sequential inputs, propagates it temporally, and outputs features, thereby achieving robust temporal feature extraction. Compared to traditional RNNs, LSTM effectively mitigates issues such as gradient vanishing and explosion, demonstrating superior capability in time-series feature extraction. The computational process for the "8 indices + 7 reflectance values" input at time step t through the LSTM layers is described as follows:

$$g_t^f = \sigma(W_{\mathrm{f}} \cdot [h_{t-1}, x_t] + b_f) \quad (13)$$

$$g_t^i = \sigma(W_{\mathrm{i}} \cdot [h_{t-1}, x_t] + b_i) \quad (14)$$

$$g_t^o = \sigma(W_{\mathrm{o}} \cdot [h_{t-1}, x_t] + b_o) \quad (15)$$

$$S_t = g_t^f \times S_{t-1} + g_t^i \times \tanh(W_c \cdot [h_{t-1}, x_t] + b_c) \quad (16)$$

$$h_t = g_t^o \times \tanh(S_t) \quad (17)$$

In the equations above, W_{f}, W_{i}, W_{o}, b_f, b_i, b_o and b_c are learnable weight matrices and bias parameters. σ 和 $\tanh$ are nonlinear activation functions. g_t^f, g_t^i, g_t^o represent the Forget Gate, Input Gate, and Output Gate vectors, respectively, responsible for selective information filtering. S_t and S_{t-1} denote the cell state vectors at time steps t−1 and t, which store and propagate temporal features extracted by the LSTM from the input time series.

The attention weights and attention-weighted hidden features are calculated as follows:

$$\alpha_t = soft\max(W_{AT} \cdot h_t + b_{AT}) \quad (18)$$

In the equation, W_{AT} and b_{AT} are learnable parameter matrices in the Attention layer. softmax is the nonlinear activation function, ensuring that the attention weights (α_1 to α_t) sum to 1 across all time steps. h^T is the hidden feature vector output by the ALSTM, representing the temporal features extracted by the HSR-SPEINet model from the meteorological factor time series.

The formula for hidden features h^S extracted by the ANN from static elevation input is as follows:

$$h_1^S = relu(W_A^1 \cdot x_S + b_A^1) \quad (19)$$

$$h_2^S = relu(W_A^2 \cdot h_1^S + b_A^2) \quad (20)$$

$$h^S = relu(W_A^3 \cdot h_2^S + b_A^3) \quad (21)$$

where $W_A^1, W_A^2, W_A^3, b_A^1, b_A^2$ and b_A^3 are the learnable parameter matrices of the first, second, and third layers of the ANN, respectively; ReLU is the nonlinear activation function; h_1^S is the hidden feature vector extracted by the first ANN layer from the elevation input x_S, h_2^S is the hidden feature vector extracted by the second ANN layer from h_1^S, and h^S is the hidden feature h_2^S extracted by the third ANN layer, which is also the final hidden feature output by the ANN from the elevation input.

Finally, the features extracted by the ALSTM and ANN are concatenated, and the MSE loss function is computed using a fully connected layer with the ground-truth SPEI values.

4. Experimental Results

This study employs deep learning techniques to acquire high-resolution environmental factors related to drought and constructs the HSR-SPEINet model. Using deep learning, high-resolution spatiotemporal drought distribution maps across China over nearly two decades and multiple temporal scales are generated.

The HSR-SPEINet model improves the spatial resolution of SPEIbase from 0.5° to 1 km. To validate the accuracy of the high spatial-resolution SPEI, data from 49 national meteorological stations in central, eastern, southern, and western China were collected. Multi-temporal-scale SPEI

values for June 2021 at these stations were calculated using the same methodology as SPEIbase. The results were compared with SPEIbase, RF SPEI from the Science Data Bank (SDB), and resampled 0.5° data from HSR-SPEINet and RF SPEI. Accuracy metrics—Pearson Correlation Coefficient (PCC), R^2, and Root Mean Square Error (RMSE)—were computed. The evaluation results are summarized in the table below:

Table 1. Accuracy evaluation for June 2021

		1 month	3 month	6 month	9 month	12 month	24 month
PCC	SPEIbase	0.8509	0.7972	0.8959	0.8939	0.9073	0.8661
	HSR-SPEINet	0.8523	0.8257	0.9026	0.8972	0.9144	0.8811
	RF SPEI	0.8725	0.6638	0.6475	0.659	0.6533	0.47
	HSR-SPEINet(0.5degree)	0.8457	0.8109	0.8931	0.9098	0.9178	0.8794
	RF SPEI(0.5degree)	0.8784	0.7647	0.7639	0.7546	0.741	0.5752
R2	SPEIbase	0.6063	0.3958	0.6513	0.6081	0.6925	0.5961
	HSR-SPEINet	0.6773	0.5913	0.7157	0.7223	0.793	0.7182
	RF SPEI	0.7593	0.4236	0.3935	0.3662	0.3444	0.0603
	HSR-SPEINet(0.5degree)	0.6747	0.5811	0.7504	0.7605	0.8038	0.7297
	RF SPEI(0.5degree)	0.7693	0.5763	0.5752	0.5671	0.5365	0.208
RMSE	SPEIbase	0.6707	0.6436	0.5457	0.5455	0.54	0.5468
	HSR-SPEINet	0.6072	0.5294	0.4927	0.4592	0.4431	0.4568
	RF SPEI	0.5244	0.6287	0.7196	0.6937	0.7885	0.8341
	HSR-SPEINet(0.5degree)	0.6097	0.5359	0.4616	0.4264	0.4314	0.4473
	RF SPEI(0.5degree)	0.5134	0.539	0.6022	0.5733	0.663	0.7657

The accuracy metrics indicate that after enhancing spatial resolution, the HSR-SPEINet model achieves slightly higher PCC and R^2 and lower RMSE compared to SPEIbase across most temporal scales. This improvement suggests that higher spatial resolution enables the model to capture more localized environmental characteristics at specific station locations, thereby better reflecting drought conditions at those sites. However, the RF SPEI dataset from SDB exhibits significant deviations from ground-truth station SPEI values. While RF SPEI shows some advantages at the 1-month time scale, its accuracy degrades sharply as the temporal scale increases.

5. Conclusions

To address the limitations of low spatial resolution in the SPEIbase dataset for high-precision drought monitoring, this study proposes the High Spatial-Resolution SPEI Network (HSR-SPEINet), a deep learning-based framework. By integrating 8 environmental factors, 7 reflectance factors, and 1 elevation dataset, the model generates a 1 km resolution SPEI product. Experimental results demonstrate that the proposed method achieves superior accuracy compared to existing public datasets when validated against ground-truth SPEI values. Future research aims to further optimize the HSR-SPEINet framework to deliver global high-resolution, high-accuracy drought monitoring products.

References

[1] Liu, Y., Zhu, Y., Ren, L. P. Singh, V., Yong, B., Jiang, S., Yuan, F., Yang, X., 2019: Understanding the Spatiotemporal Links Between Meteorological and Hydrological Droughts From a Three-Dimensional Perspective. *Journal of Geophysical Research: Atmospheres* 124(6), 3090-3109.

[2] Wang, Z., Wang, J., Wang, J. 2015: Risk Assessment of Agricultural Drought Disaster in SouthernChina. *Discrete Dynamics in Nature and Society*, 2015, 1-8.

[3] AMS, 1997: Meteorological drought-Policy statement. *Bulletin of American Meteorological Society* 78(5), 847-849.

[4] Zhang, T., Su, X., Zhang, G., Wu, H., Wang, G., Chu, J., 2022: Evaluation of the impacts of human activities on propagation from meteorological drought to hydrological drought in the Weihe River Basin, China. *The Science of the total environment* 819, 153030-153030.

[5] Kogan, F., Adamenko, T., Guo, W., 2013: Global and regional drought dynamics in the climate warming era. *Remote Sensing Letters* 4(4), 364-372.

[6] Wilhite, D. A., Svoboda, M. D., Hayes, M. J., 2007: Understanding the complex impacts ofdrought: A key to enhancing drought mitigation and preparedness. *WaterResources Management* 21(5), 763-7.

[7] Shi, J., Liu, M., Li, Y., Guan, C., 2025: Response of total primary productivity of vegetation to meteorological drought in arid and semi-arid regions of China. *Journal of Arid Environments* 228, 105346-105346.

[8] Han, L., Camarero, J. J., Jia, G., Zhang, Z., Chen, L., 2025: Drought resilience and legacy effects in two forest tree species on Loess Plateau of China: Growth and water-use efficiency under different drought conditions. *Forest Ecosystems* 13, 100297-100297.

[9] Mackay, A., 2008: Climate Change 2007: Impacts, Adaptation and Vulnerability. Contribution of Working Group II to the Fourth Assessment Report of the Intergovernmental Panel on Climate Change. *Journal of Environmental Quality* 37(6), 2407-2407.

[10] Zhan, Y., Ma, C., Yan, Y., Luo, Y., Wang, X., Wang, S., Rong, Y., 2025: The study of the response regularity of photosynthesis to flash drought in different vegetation ecosystems of the middle and lower reaches of the Yangtze River Basin. *International journal of biometeorology* (prepublish), 1-14.

[11] Wen, D., Cao, J., 2025: Copula-based interannual variability of winter-spring hot drought events over the low-latitude highlands of China. *Journal of Hydrology* 654, 132936-132936.

[12] Zhu, R., Jiang, Y., Wang, B., Zhang, Y., 2025: Changes in human settlement environments and their drivers in valley cities located in arid and semi-arid regions: A case study of Lanzhou

in Western China. *Research in Cold and Arid Regions* 16(3), 149-158.
[13] Yang, X., Liao, X., Di, D., Shi, W., 2023: A Review of Drought Disturbance on Socioeconomic Development. *Water* 15(22).
[14] McKee, T. B., Doesken, N. J., Kleist, J., 1993: The relationship of drought frequency and duration to time scales. *Proceedings of the 8th Conference on Applied Climatology* 17(22), 179-183.
[15] Vicente-Serrano, S. M., Beguería, S., López-Moreno, J. I., 2010: A Multiscalar Drought Index Sensitive to Global Warming: The Standardized Precipitation Evapotranspiration Index. *Journal of Climate* 23(7), 1696-1710,1712,1714-1718.
[16] Palmer, W. C., 1965: Meteorological droughts. *U. S. Departmcnt of commerce weather bureau research paper* 45(58), 23- 26.
[17] Sunusi, N., Auliana, H. N., 2025: Assessing SPI and SPEI for drought forecasting through the power law process: A case study in South Sulawesi, Indonesia. *MethodsX* 14, 103235-103235.
[18] Vahedi, J., Ghahremanzadeh, M., Pishbahar, E., Dashti, G., Samadianfard, S., 2025: Saffron price dynamics in Iran: Influence of the standardized precipitation index with Copula functions. *Journal of Cleaner Productio*n 495, 145009-145009.
[19] Brands, S., Iturbide, M., Pardo, G. D., J., Herrera, S., Bedia, J., Manzanas, R., Guisado, R. E., Beguería, S., Serrano, V. M. S., Gutiérrez, M. J., 2025: Seasonal drought predictions in the Mediterranean using the SPEI index: Paving the way for their operational applicability in climate services. *Climate Services* 38, 100555-100555.
[20] Trevino, M. A., Stine, R. A., Huybers, P., 2021: Regional Nonlinear Relationships Across the United States Between Drought and Tree-Ring Width Variability From a Neural Network. *Geophysical Research Letters* 48(14), e2020GL092090-e2020GL092090.
[21] Moradi, E., Khosravi, H., Rahimabadi, D. P., Choubin, B., Muchová, B., 2024: Integrated approach to land degradation risk assessment in arid and semi-arid Ecosystems: Applying SVM and eDPSIR/ANP methods. *Ecological Indicators* 169, 112947-112947.
[22] Oruc, S., Hinis, A. M., Tugrul, T., 2024: Evaluating Performances of LSTM, SVM, GPR, and RF for Drought Prediction in Norway: A Wavelet Decomposition Approach on Regional Forecasting. *Water* 16(23), 3465-3465.
[23] Banik, R., Biswas, A., 2024: Rainfall prediction for climate-resilient agriculture: a robust ensemble with SARIMA and LightGBM. *Paddy and Water Environment* (prepublish), 1-13.
[24] Muhammad, R. A., Liang, H. D., R., R. M., Md, A. I., I, T., Ozgur, K., Salim, H., Mohammad, K. Z., 2023: Modelling groundwater level fluctuations by ELM merged advanced metaheuristic algorithms using hydroclimatic data. *Geocarto International* 38(1).
[25] Shen, R., Huang, A., Li, B., Guo, J., 2019: Construction of a drought monitoring model using deep learningbased on multi-source remote sensing data. *International Journal of Applied EarthObservation and Geoinformation* 79, 48-57.
[26] Achite, M., Katipoğlu, M. O., Jehanzaib, M., Kartal, V., Mansour, H., 2024: Understanding run theory for evaluating hydrologic drought in the Wadi Mina Basin (Algeria): A historical analysis. *Theoretical and Applied Climatology* (prepublish), 1-16.
[27] Zhang, Z., Xu, W., Shi Z., Qin, Q., 2021: Establishment of a Comprehensive Drought Monitoring IndexBased on Multisource Remote Sensing Data and Agricultural Drought Monitoring. *IEEE Journal of Selected Topics in Applied Earth Observations and Remote Sensing* 14, 2113-2126.
[28] Prodhan, F. P., Zhang, J., Yao, F., Shi, L., Prasad, T. S. P., Zhang, D., Cao, D., Zheng, M., Ahmed, N., Mohana, H. P., 2023: Deep Learning for Monitoring Agricultural Drought in South AsiaUsing Remote Sensing Data. *Remote Sensing* 13 (9), 1715-1715.
[29] Balti, H., Abbes, A. B., Mellouli, N., Sang, Y., Farah, I. R., Lamolle, M., Zhu, Y., 2021: Big data based architecture for drought forecasting using LSTM, ARIMA, and Prophet: Case study of the Jiangsu Province, China. *2021 International Congress of Advanced Technology and Engineering (ICOTEN)*, 1-8.
[30] Morgan, H., Elgendy, A., Said, A., Hashem, M., Li, W., Maharja, S., Askary, E. H., 2024: Enhanced lithological mapping in arid crystalline regions using explainable AI and multi-spectral remote sensing data. *Computers and Geosciences* 193, 105738-105738.
[31] Zhu, F., Wang, J., Lv, P., Qiao, X., He, M., He, Y., Zhao, Z., 2024: Generating labeled samples based on improved cDCGAN for hyperspectral data augmentation: A case study of drought stress identification of strawberry leaves. *Computers and Electronics in Agriculture* 225, 109250-109250.
[32] Lazić, O., Cvejić, S., Dedić, B., Kupusinac, A., Jocić, S., Miladinović, D., 2024: Transfer Learning in Multimodal Sunflower Drought Stress Detection. *Applied Sciences* 14(14), 6034-6034.
[33] Gao, S., Liang, H., Hu, D., Hu, X., Lin, E., Huang, H., 2024: SAM-ResNet50: A Deep Lear ning Model for the Identification and Classification of Drought Stress in the Seedling Stage of Betula luminifera. *Remote Sensing* 16(22), 4141-4141.
[34] Wei, Q., Yang, J., Fu, F., Xue, L., 2025: Dynamic classification and attention mechanism-based bidirectional long short-term memory network for daily runoff prediction in Aksu River basin, Northwest China. *Journal of Environmental Management* 374, 124121-124121.